Draft version March 15, 2021
Typeset using LaTeX **preprint2** style in AASTeX63

Small-Scale Dynamo in Supernova-Driven Interstellar Turbulence

Frederick A. Gent,[1,2] Mordecai-Mark Mac Low,[3,4] Maarit J. Käpylä,[1,5,6] and Nishant K. Singh[7,5]

[1] *Astroinformatics, Department of Computer Science, Aalto University, PO Box 15400, FI-00076 Espoo, Finland*
[2] *School of Mathematics, Statistics and Physics, Newcastle University, NE1 7RU, UK*
[3] *Department of Astrophysics, 79th Street at Central Park West, American Museum of Natural History, New York, NY 10024, USA*
[4] *Center for Computational Astrophysics, 162 Fifth Avenue, Flatiron Institute, New York, NY 10010, USA*
[5] *Max Planck Institute for Solar System Research, Justus-von-Liebig-Weg 3, 37707 Göttingen, Germany*
[6] *Nordic Institute for Theoretical Physics, Roslagstullsbacken 23, 106 91 Stockholm, Sweden*
[7] *Inter-University Centre for Astronomy & Astrophysics, Post Bag 4, Ganeshkhind, Pune 411 007, India*

(Received October 4, 2020; Revised March 15, 2021; Accepted)

Submitted to ApJL

ABSTRACT

Magnetic fields grow quickly even at early cosmological times, suggesting the action of a small-scale dynamo (SSD) in the interstellar medium of galaxies. Many studies have focused on idealized turbulent driving of the SSD. Here we simulate more realistic supernova-driven turbulence to determine whether it can drive an SSD. Magnetic field growth occurring in our models appears inconsistent with simple tangling of magnetic fields, but consistent with SSD action, reproducing and confirming models by Balsara et al. (2004) that did not include physical resistivity η. We vary η, as well as the numerical resolution and supernova rate, $\dot{\sigma}$, to delineate the regime in which an SSD occurs. For a given $\dot{\sigma}$ we find convergence for SSD growth rate with resolution of a parsec. For $\dot{\sigma} \simeq \dot{\sigma}_{\rm sn}$, with $\dot{\sigma}_{\rm sn}$ the solar neighbourhood rate, the critical resistivity below which an SSD occurs is $0.005 > \eta_{\rm crit} > 0.001\,{\rm kpc}^{-1}\,{\rm km\ s}^{-1}$, and this increases with the supernova rate. Across the modelled range of 0.5–4 pc resolution we find that for $\eta < \eta_{\rm crit}$, the SSD saturates at about 5% of kinetic energy equipartition, independent of growth rate. In the range $0.2\,\dot{\sigma}_{\rm sn} \le \dot{\sigma} \le 8\,\dot{\sigma}_{\rm sn}$ growth rate increases with $\dot{\sigma}$. SSDs in the supernova-driven interstellar medium commonly exhibit erratic growth.

Keywords: dynamo — magnetohydrodynamics (MHD) — ISM: supernova remnants — ISM: magnetic fields — turbulence

Corresponding author: Maarit Käpylä
Email: frederick.gent@aalto.fi, mordecai@amnh.org, maarit.kapyla@aalto.fi, nishant@iucaa.in

1. INTRODUCTION

We here study the small-scale dynamo (SSD) in the interstellar medium (ISM). SSD acts at small eddy scales of turbulence, driving

magnetic field growth at correspondingly short timescales. The large-scale dynamo (LSD) with much longer turnover times generates magnetic fields ordered on kiloparsec scales. Hence, capturing LSD alongside the faster growing modes of SSD in simulations is computationally challenging. However, interaction between SSD and LSD modes likely fundamentally determines the evolution and structure of the magnetic field.

Many simulations of supernova- (SN)-driven turbulence with realistic vertical stratification (e.g., de Avillez & Breitschwerdt 2005; Piontek & Ostriker 2007; Hill et al. 2012; Hennebelle & Iffrig 2014) have no mechanism to induce LSD, such as rotation and shear. Strong ordered magnetic field effects are modelled by imposition of a background, typically uniform, magnetic field. Some large-scale models do seek to include LSD (e.g., Korpi et al. 1999; Gressel et al. 2008; Hanasz et al. 2009; Wang & Abel 2009; Pakmor et al. 2017; Gressel & Elstner 2020), but show no SSD, or appear to find SSD within the context of halo-disk scale flows (e.g., Rieder & Teyssier 2016; Steinwandel et al. 2019), but capture no LSD. Gent et al. (2013a, with additional analysis by Evirgen et al. 2017) appear to include an SSD with an LSD. To confirm this and determine its effect on LSD, we must understand the properties of the SSD.

Any magnetic noise produced by tangling of a large-scale field will also grow exponentially if an LSD is present. This noise can play an important role in quenching the LSD. We need to discriminate this effect from an SSD.

Previous experiments (e.g., Balsara et al. 2004, hereafter BKMM4; Balsara & Kim 2005; Mac Low et al. 2005) examined the SN-driven SSD. The limited resolution study of BKMM4 did not allow demonstration of solution convergence. Furthermore, they imposed a uniform background field and implemented no physical resistivity or viscosity. We shall show that the amplification of their field is a result of SSD action and not just tangling of the field.

In this Letter we first compare the SSD to tangling in an idealized simulation (Sect. 2). We then describe our models of SN-driven turbulence for demonstrating the action of SSD (Sect. 3). Simulations use the PENCIL CODE[1]. A broad resolution and parameter study allows us to show numerical convergence and determine the critical resistivity for excitation of an SSD, which we follow to saturation (Sect. 4). This provides objective criteria for the action of SSD in simulations (such as Gent et al. 2013a; Gressel & Elstner 2020; Steinwandel et al. 2019). Finally, we conclude in Sect. 5.

2. DISENTANGLING THE DYNAMO

Previous SSD studies have examined Pm dependence with stochastic nonhelical forcing, including at high Mach number (e.g., Haugen et al. 2003, 2004a,b; Federrath et al. 2011, 2014). Here we specifically seek to illustrate differences between tangling and SSD. Nonhelical random forcing is applied at wavenumber $k_\mathrm{f}/k_1 = 8$ to 256^3 zone, 2π-periodic, isothermal boxes with viscosity $\nu = 5 \cdot 10^{-3}$. The lowest wavenumber in the domain is $k_1 = 1$ and the largest is the Nyquist frequency $k/k_1 = 128$. The imposed uniform field has $e_B \simeq 6{\cdot}10^{-22}\,\overline{e_K}$, where $\overline{e_K}$ is the time-averaged kinetic energy density.

Two simulations are distinguished by use of dimensionless resistivity $\eta = 10^{-4}$ and $\eta = 2 \cdot 10^{-3}$. Respectively, these yield magnetic Reynolds number $\mathrm{Rm} = 150$, with magnetic Prandtl number $\mathrm{Pm} = 50$, exciting an SSD and $\mathrm{Rm} = 7.4$, with $\mathrm{Pm} = 2.5$, inhibiting the dynamo so that amplification is limited to tangling of the imposed field.

[1] https://github.com/pencil-code

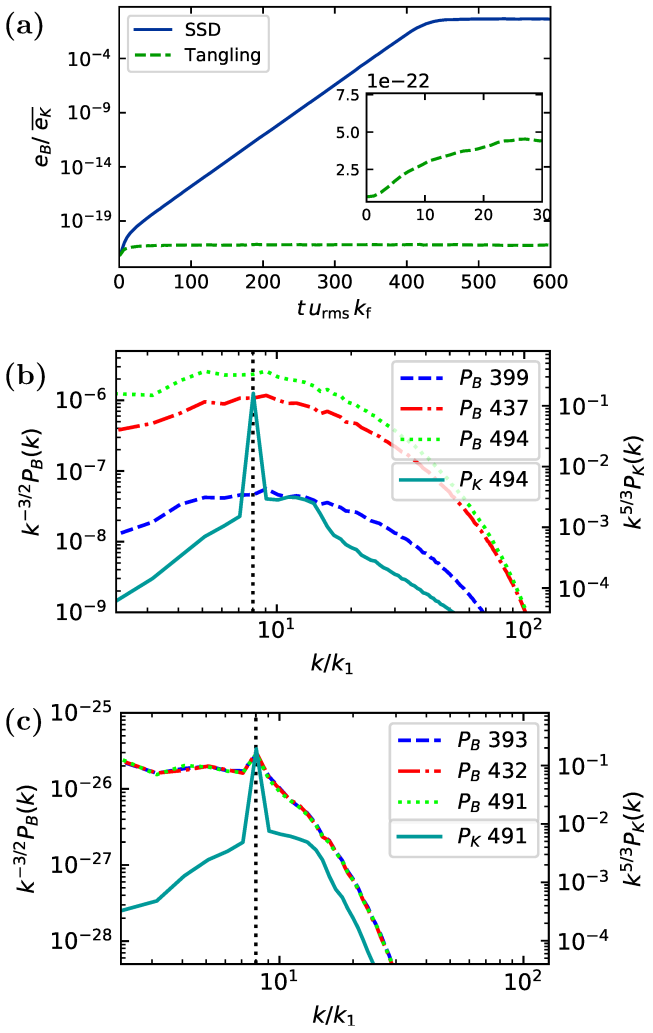

Figure 1. (a) Mean magnetic energy density, e_B, with nonhelical random forcing, scaled to time-averaged kinetic energy density, $\overline{e_K}$. Inset: early zoom-in of linear growth of tangled field. Time is normalised by eddy turnover time, $1/k_{\rm f}u_{\rm rms}$. Compensated power spectra of kinetic energy P_k and magnetic energy P_B for (b) SSD and (c) tangling, at times given in the legends. Kinetic energy uses the right-hand axes. Forcing scale, $k_{\rm f}/k_1 = 8$: vertical dotted line.

Figure 1 (a) shows the SSD growing exponentially in just over 400 eddy turnover times; see Zeldovich et al. (1983) for SSD properties and excitation conditions. Tangling induces only linear growth (see inset), saturating just above the imposed field energy within 50 turnover times.

Figures 1(b) and 1 (c) show compensated power spectra for both cases. Magnetic energy spectra are compensated for by Kazantsev's $k^{3/2}$ power law (Schekochihin et al. 2002; Bhat & Subramanian 2014), and kinetic energy by Kolmogorov's $k^{-5/3}$. The forcing scale $k_{\rm f}$ is prominent in the magnetic energy spectra of the tangling but not in the magnetic spectra of the SSD. For SSD the range with Kazantsev power law (horizontal) extends to scales smaller than the forcing scale (Figure 1 b), and during the kinematic phase the magnetic energy peak is at $k/k_1 \simeq 9$. For tangling (Figure 1 c) the Kazantsev scaling applies only at $k/k_1 < k_{\rm f}$. Thus, in the SSD, kinetic energy in the Kolmogorov cascade transfers to magnetic energy at these scales, inducing an inverse Kazantsev cascade at scales smaller than $k_{\rm f}$, while tangling transfers energy only at scales between $k_{\rm f}$ and the scale of the imposed field.

3. SUPERNOVA-DRIVEN TURBULENCE MODEL DESIGN

Our SN-driven turbulence models exclude large-scale magnetic field dynamics by omitting global-scale rotation, shear, and stratification. Our simulation domain is a periodic cube of length 256 pc and zone size $\delta x = 0.5$, 1, 2 or 4 pc, except for our direct comparisons with BKMM4, which have domains of 200 pc and $\delta x = 0.78$, 1.56 and 3.12 pc (units henceforth assumed). Our fiducial models exclude tangling of an imposed field as a source of magnetic amplification, by applying a random 10 nG initial field. Transient dissipation prior to hydrodynamic steady state and dynamo onset yields a turbulent seed field of about 1 nG. For models reproducing BKMM4 this seed is substituted by a uniform 10 nG background field as applied by BKMM4.

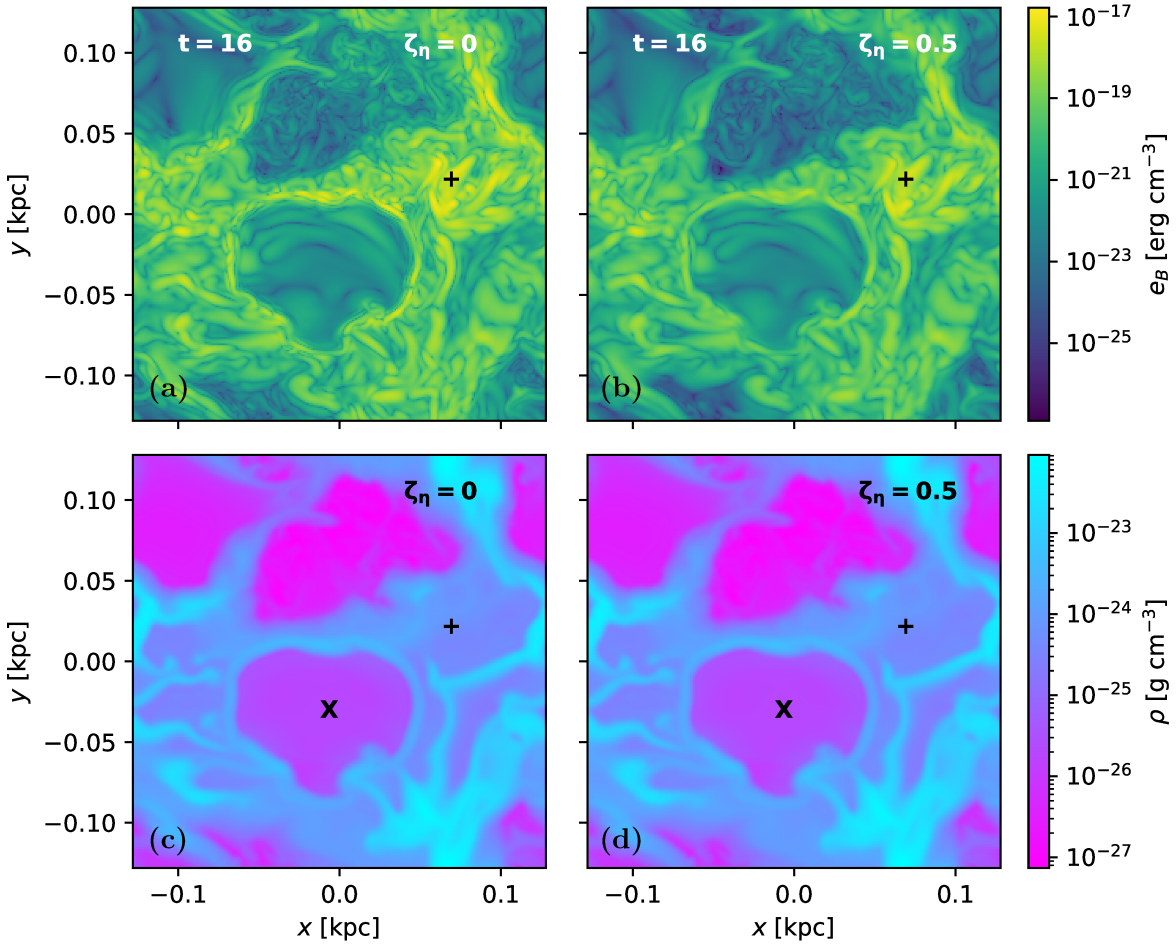

Figure 2. 2D slices of (a, b) magnetic energy density e_B and (c, d) gas density with shock dependent resistivity, ζ_η, as indicated. The site of the most recent SN is indicated by X (c, d). $\delta x = 1\,\mathrm{pc}$, $\eta = 10^{-4}$ and $\nu = 10^{-3}$ km s^{-1} kpc^{-1}.

We solve the system of non-ideal, compressible, non-isothermal MHD equations

$$\frac{D\rho}{Dt} = -\rho\boldsymbol{\nabla}\cdot\boldsymbol{u} + \boldsymbol{\nabla}\cdot\zeta_D\boldsymbol{\nabla}\rho, \tag{1}$$

$$\begin{aligned}\rho\frac{D\boldsymbol{u}}{Dt} = {}& \boldsymbol{\nabla}E_{\rm kin}\sigma - \rho c_{\rm s}^2\boldsymbol{\nabla}\left(s/c_{\rm p} + \ln\rho\right) + \boldsymbol{j}\times\boldsymbol{B} \\ & + \boldsymbol{\nabla}\cdot\left(2\rho\nu\mathbf{W}\right) + \rho\,\boldsymbol{\nabla}\left(\zeta_\nu\boldsymbol{\nabla}\cdot\boldsymbol{u}\right) \\ & + \boldsymbol{\nabla}\cdot\left(2\rho\nu_3\mathbf{W}^{(3)}\right) - \boldsymbol{u}\boldsymbol{\nabla}\cdot\left(\zeta_D\boldsymbol{\nabla}\rho\right),\end{aligned} \tag{2}$$

$$\begin{aligned}\rho T\frac{Ds}{Dt} = {}& E_{\rm th}\dot{\sigma} + \rho\Gamma - \rho^2\Lambda + \eta\mu_0\boldsymbol{j}^2 \\ & + 2\rho\nu\left|\mathbf{W}\right|^2 + \rho\,\zeta_\nu\left(\boldsymbol{\nabla}\cdot\boldsymbol{u}\right)^2 \\ & + \boldsymbol{\nabla}\cdot\left(\zeta_\chi\rho T\boldsymbol{\nabla}s\right) + \rho T\chi_3\boldsymbol{\nabla}^6 s \\ & - c_{\rm v}\,T\left(\zeta_D\nabla^2\rho + \boldsymbol{\nabla}\zeta_D\cdot\boldsymbol{\nabla}\rho\right),\end{aligned} \tag{3}$$

$$\frac{\partial\boldsymbol{A}}{\partial t} = \boldsymbol{u}\times\boldsymbol{B} + \eta\boldsymbol{\nabla}^2\boldsymbol{A} + \eta_3\boldsymbol{\nabla}^6\boldsymbol{A}, \tag{4}$$

with the ideal gas equation of state closing the system. Most variables take their usual meanings. Terms containing $\zeta_D = 2$, $\zeta_\nu = 5$ and $\zeta_\chi = 2$ are applied to all ISM models and resolve shock discontinuities with artificial diffusion of mass, momentum, and energy proportional to shock strength (see Gent et al. 2020, for details). Equations (2) and (3) include terms with ζ_D to provide momentum and energy conserving corrections for the artificial mass diffusion applying in Equation (1). In previous work Gent et al. (2013a) we have used a formalism that included artificial diffusion in vector potential

at shocks. In Figure 2 we show comparative slices of the magnetic energy and gas density with and without resistive shock diffusion ζ_η. With $\zeta_\eta > 0$ (Fig. 2 b) magnetic energy is reduced in the remnant shell relative to Figure 2 a, where compression actually enhances it. Since the magnetic field is well resolved in either case, as also shown by the magnetic energy spectra below, and the simulation is numerically stable without it, this extra artificial diffusion is unnecessary.

In both models a concentration of magnetic energy, marked with + in Figure 2, has below average gas density. This snapshot reflects the overall behaviour of the system, in which magnetic field amplification also occurs independently of shock compression. As Figure 2 shows, SN shock fronts do compress and amplify the magnetic field, resulting in strong local and instantaneous correlation of the field and density. However, on global and long-term scale, this is not the dominant mechanism for the dynamo, which operates just as effectively in the non-shocked, more diffuse regions, as is also indicated by this figure. This is based on the amplification factor due to compression being estimated $\lesssim 2$, taken as density fluctuations to power 4/3, while the magnetic energy is amplified by 4–6 orders of magnitude.

Unlike past experiments (Gent et al. 2013a,b, 2020), thermal diffusivity χ is also omitted, as the artificial diffusivities chosen are adequate to ensure numerical stability. The physical effects of thermal conductivity can be expected to be relevant only at the unresolved or marginally resolved Field length defined by Begelman & McKee (1990, named after George Field, not the magnetic field). Terms containing ν_3, χ_3 and η_3 apply sixth-order hyperdiffusion to resolve grid-scale instabilities (see, e.g., Brandenburg & Sarson 2002; Haugen & Brandenburg 2004), with mesh Reynolds number set to be $\simeq 1$ for each δx.

The simplified isothermal model considered in Sect. 2 solves only Equations (1), (2) and (4), without the shock-dependent diffusion or hyperdiffusion terms, and while setting $\boldsymbol{B} = \boldsymbol{\nabla} \times \boldsymbol{A} + \boldsymbol{B}_{\rm imposed}$.

In the ISM simulations SNe are exploded at uniform random positions at a Poisson rate $\dot{\sigma}$ scaled by the solar neighborhood value $\dot{\sigma}_{\rm sn} \simeq 50$ kpc^{-3} Myr^{-1}. Explosions inject $E_{\rm th} = 10^{51}$ erg thermal energy, except in dense regions, where a proportion ($< 5\%$) may be kinetic $E_{\rm kin}$ (see Gent et al. 2020). Models with common $\dot{\sigma}$ have the same timing and location of explosions. Non-adiabatic heating Γ and cooling $\Lambda(T)$ are included (Gent et al. 2013a) following Wolfire et al. (1995) and Sarazin & White (1987).

To understand the effects of purely numerical diffusivity, we also run an ideal MHD model with $\eta = 0$ and $\nu = 0$. We determine how low a physical resistivity η can be resolved by varying it from 10^{-5} to 10^{-3} kpc km s^{-1} (units assumed henceforth). We also test the effect of ${\rm Pm} = \nu/\eta$, varying ν with $\eta = 10^{-4}$ or varying η with $\nu = 10^{-3}$. Our direct comparison with the results of BKMM4 uses Pm = 2.5, apart from one run using $\eta = \nu = 0$.

4. RESULTS

4.1. *Resolution and convergence*

Figure 3 shows that numerical diffusion still dominates at studied resolutions for resistivity $\eta = 10^{-4}$, as can be seen from the increasing speed of the SSD with resolution, but that a converged SSD solution emerges at $\eta = 10^{-3}$ for parsec resolution. Saturation at around 5% of $\overline{e_K}$ appears to be a well-converged result. The $\eta = 10^{-3}$ models show false convergence (Fryxell et al. 1991) of solutions with similar magnetic energy decay at $\delta x \geq 2$. We note that strong fluctuations in the characteristics of the flow occur at the low $\dot{\sigma}$ that we choose to avoid thermal runaway (Li et al. 2015), with thermal phases occupying changing fractional volumes

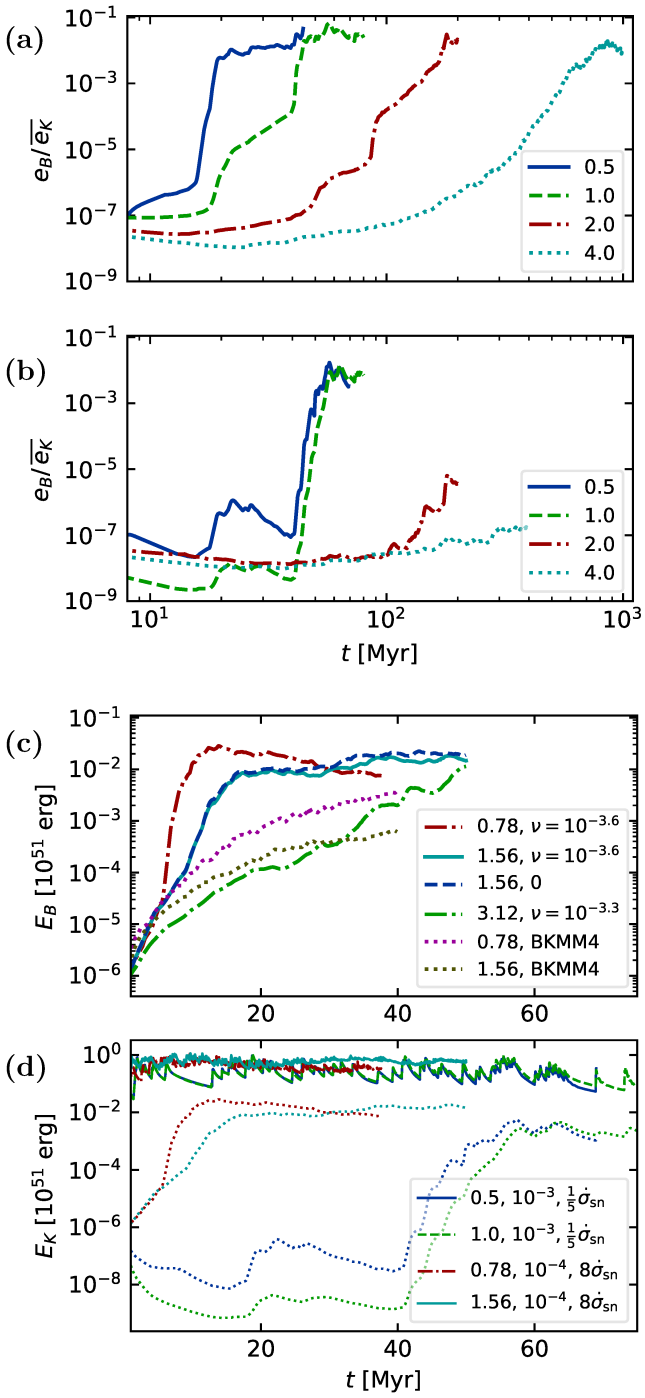

Figure 3. Magnetic energy density shown for resolutions δx given in the legends for models with resistivity (a) $\eta = 10^{-4}$, and (b) $\eta = 10^{-3}$, scaled by the time-averaged kinetic energy density $\overline{e_K}$. Total magnetic energy, E_B scaled by $E_{\rm th}$, (c) matching BKMM4 for δx and viscosity ν included in the legend and (d) kinetic energy, E_K, for δx, η and $\dot{\sigma}$ given in the legend with corresponding magnetic energy (dotted).

(e.g. Gatto et al. 2015) and hosting SSD instabilities with different thresholds and growth rates.

We ran models to reproduce the results of BKMM4, which adopt their choice $\dot{\sigma} = 8\dot{\sigma}_{\rm sn}$. In our fiducial runs we use a lower value of $0.2\dot{\sigma}_{\rm sn}$ to preserve multiphase thermal structure. The higher $\dot{\sigma}$ rapidly drives thermal runaway resulting in high temperatures $T > 10^7$ K. The growth rate is faster than in our fiducial models (Figure 3 (c)), reflective of the single phase kinematics and more persistent forcing rate, yet still saturating at about 5% of $\overline{e_K}$. At equivalent resolution, the sixth-order Pencil Code has far lower diffusion than the second-order Godunov code used by BKMM4. As a result, we find faster growth at equivalent resolution. Figure 3(d) shows that kinetic energy fluctuates around a stationary mean in our models, with higher SN rate $\dot{\sigma}$ producing higher kinetic energy, less intermittency in the energy, and less erratic growth in the dynamo.

We can also examine the kinetic and magnetic energy spectra (Figure 4). The kinetic spectra for $\delta x \leq 1$ agree well at all scales above the viscous cutoff, which appears, as expected, at lower k for $\delta x = 1$ than $\delta x = 0.5$. By contrast the kinetic spectra for $\delta x \geq 2$ differ and exhibit significant energy losses at all scales, indicating only solutions for $\delta x \lesssim 1$ have converged.

The addition of viscosity $\nu = 10^{-3}$, indicated by the magenta curves in panels (b) and (c), makes little difference to the shape of the magnetic or kinetic energy spectra. The magnitude of the magnetic energy spectrum increases somewhat with the addition of viscosity, as can also be seen from comparing dotted light and dark blue lines in Figure 5 (a2).

We have shown that SSD turbulence converges for $\delta x \leq 1$. Underresolving SN driven turbulence results in a significant loss of energy at all scales. The SSD for $0.2\dot{\sigma}_{\rm sn} \leq \dot{\sigma} \leq 8\dot{\sigma}_{\rm sn}$

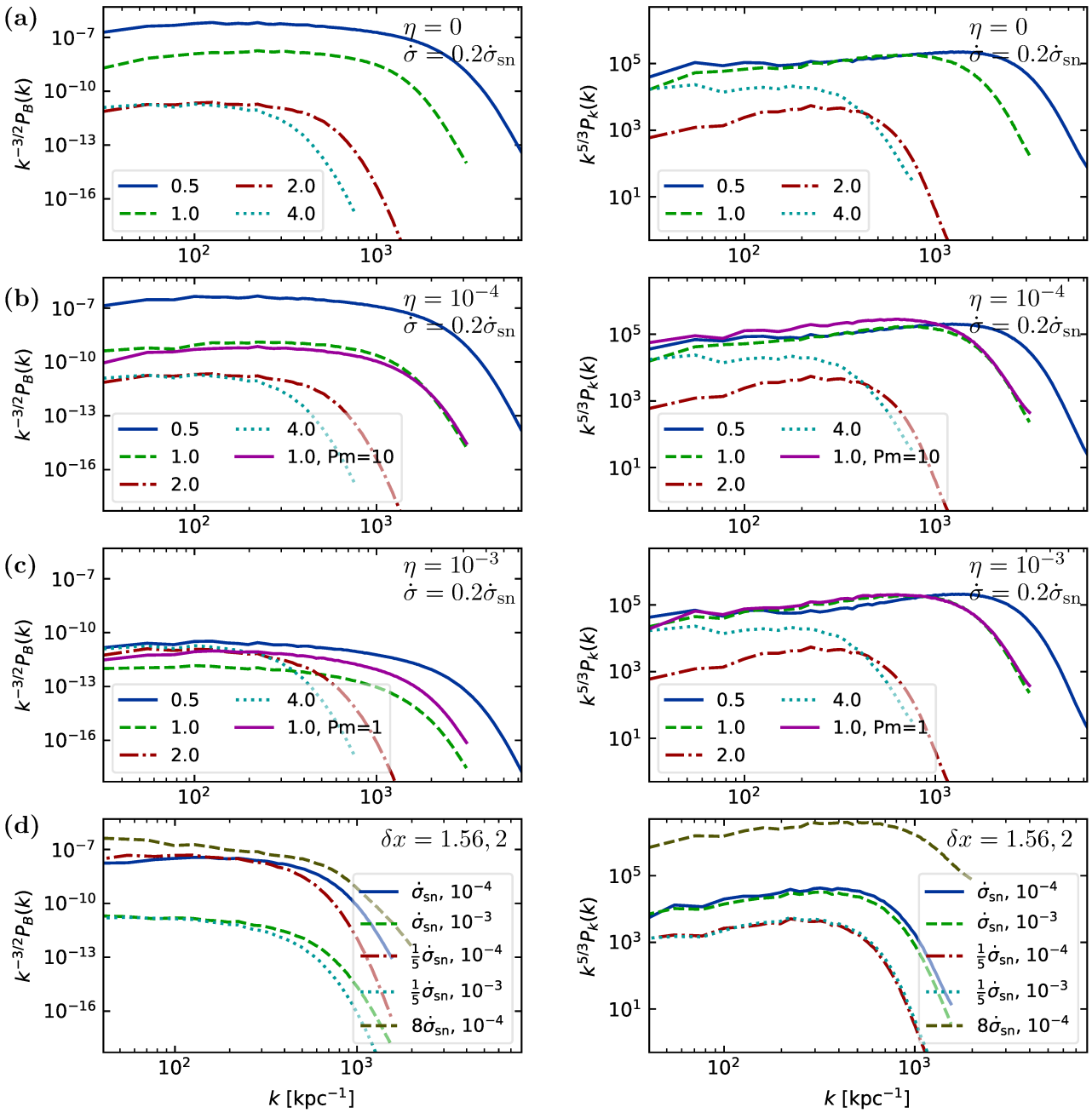

Figure 4. Compensated magnetic (left) and kinetic (right) energy spectra. Compensation is for the Kazantsev spectrum $k^{3/2}$ (left) or the Kolmogorov spectrum $k^{-5/3}$ (right). (a)–(c): Samples at $t = 27.5$ Myr for δx given in the legend for resistivity η and supernova rate $\dot{\sigma}$ as indicated on each panel. Field strengths reached differ between models at this time (see Fig. 3). Viscosity $\nu = 0$, except $\nu = 10^{-3}$ for models identified by Pm. (d): Samples taken at different times but similar field strength at η and $\dot{\sigma}$ as indicated in the legend, with the highest supernova rate being the $\delta x = 1.56$ run from the comparison with BKMM4 and $\delta x = 2$ otherwise.

saturates in the ISM at about 5%$\overline{e_K}$ and grows more rapidly with increasing SN rate.

4.2. *Effective resistivity and Prandtl number*

To understand the role of physical resistivity η and viscosity ν on the SSD, we need to determine the value at each resolution where they exceed numerical diffusion in strength. Figure 5 shows that a physical resistivity of $\eta = 10^{-5}$ (panels a1, a2) makes no impact on field growth at $\dot{\sigma} = 0.2\dot{\sigma}_{\rm sn}$, while $\eta = 10^{-3}$ clearly dominates over numerical resistivity at all resolutions. The exact value of the minimum physical resistivity does seem to vary not just with δx but also with σ, as can be seen by comparison of the $\eta = 10^{-4}$ and 10^{-3} cases (panels c1 to d2).

When we consider e_B for the models with only numerical viscosity (Fig 5 a, c, d), $\eta \geq 10^{-3}$ initially appears sufficient to suppress SSD. At low resolution this remains so for $\dot{\sigma} = 0.2\dot{\sigma}_{\rm sn}$ (panels c1 and d1), apart from a transitory surge near 100 Myr for $\delta x = 2$. However, for $\dot{\sigma} = \dot{\sigma}_{\rm sn}$ within 100 Myr SSD is evident. Only, $\eta = 0.005$ dampens SSD (panel d2).

The kinetic energy spectra in Figure 4 may show the resolution of this contradiction. They display a bottleneck effect (Falkovich 1994; Haugen et al. 2003), an energy cascade less efficient than $k^{-5/3}$ leading to an accumulation of power and then rapid dissipation at high k. This bottleneck shifts to lower k as δx increases (panels a–c) or $\dot{\sigma}$ decreases (panel d). The deeper into the magnetic energy spectrum this peak extends, the more scales available for transfer to magnetic energy and the more efficient the SSD. The critical resistivity above which SSD is suppressed, therefore, increases with $\dot{\sigma}$, within the range considered. Even at $\dot{\sigma} = 0.2$, for $\eta = 10^{-3}$ and $\delta x \leq 1$ SSD occurs after 20 – 40 Myr.

Resistivity contributes to Rm, which is expected to control the onset of the SSD and affect growth rate. We therefore anticipate that lower η would correlate with higher growth rate (Schekochihin et al. 2007). This mainly is the case when we compare models with $\delta x \leq 1$ at concurrent stages in their evolution. However, in Figure 5 (c2) there are some anomolous patterns, where higher η models overtake lower η models, e.g., at 80 Myr. To explore this further we include experiments with $\delta x = 1$ and $\nu > 0$, and examine the effect of Pm on the SSD (Figure 5 b1, b2). We identify each model by Pm $= \nu/\eta$, but due to the inclusion of shock and hyper diffusivities, the effective Pm and, indeed, Rm vary substantially across space and time. In b1 we include one run with shock resistivity, $\zeta_\eta \neq 0$ (olive, dashed), which is referenced in Figure 2. The dynamo is slower and saturates lower than the comparative model Pm $= 10$ (blue, solid). This is consistent with more efficient dissipation of compressed field.

Plotted in panel b2, where we fix $\eta = 10^{-4}$ and vary ν, initial growth of e_B is faster for Pm $= 0.1$ than for higher values. This is a regime *less* conducive to exciting the SSD than the high Pm regime typical of the ISM (Haugen et al. 2004a). A plausible explanation may be that the higher fluid Reynolds number, Re, could facilitate the dynamo. We therefore set a physical viscosity $\nu = 10^{-3}$ and vary η. Plotted in panel (b1) the growth rates mainly conform to our expectations, except for Pm $= 5$ between 20 and 40 Myr. We confirm that $\eta \geq 10^{-2.3}$ suppresses SSD at $\dot{\sigma} = 0.2\dot{\sigma}_{\rm sn}$. While the saturation level is insensitive to Pm, with ν fixed (panel b2), the saturation level increases with Pm for η fixed (panel b1), indicating saturation level is sensitive to Re. We also include two of these plots in panel (a2) for comparison to $\nu = 0$. Comparing the kinetic energy spectra (magenta) models in Figure 4 (b2, c2), ν alters very little.

We have shown that the critical resistivity for SSD in the ISM with a low SN rate is $10^{-2.3} > \eta_{\rm crit} > 10^{-3}$ and that this increases with increasing $\dot{\sigma}$ within the range considered. Although higher Rm and Pm generally increase

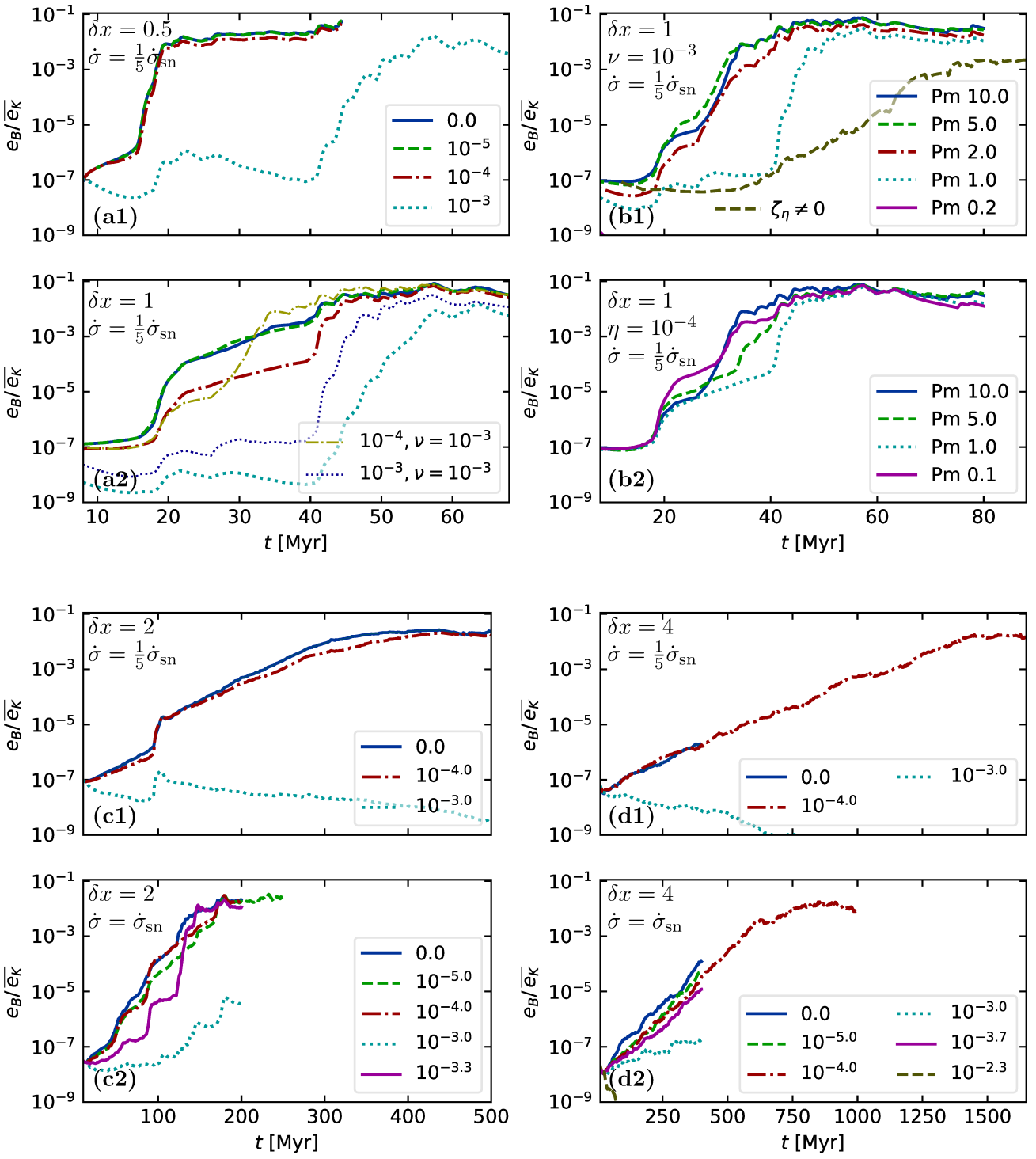

Figure 5. Magnetic energy density e_B normalized by the time-averaged kinetic energy $\overline{e_K}$ for values given in each panel of resolution δx and SN rate $\dot{\sigma}$. Time axes extend for $\delta x \geq 2$ to accommodate SSD saturation. Captions indicate resistivity η, with viscosity $\nu = 0$, unless indicated otherwise or where $\mathrm{Pm} = \nu/\eta$ is varied with ν fixed (b1) or η fixed (b2). In (b1) the run with $\zeta_\eta = 0.55$ has $\mathrm{Pm} = 10$. All other models have $\zeta_\eta = 0$. Line styles in (a1) also apply in (a2).

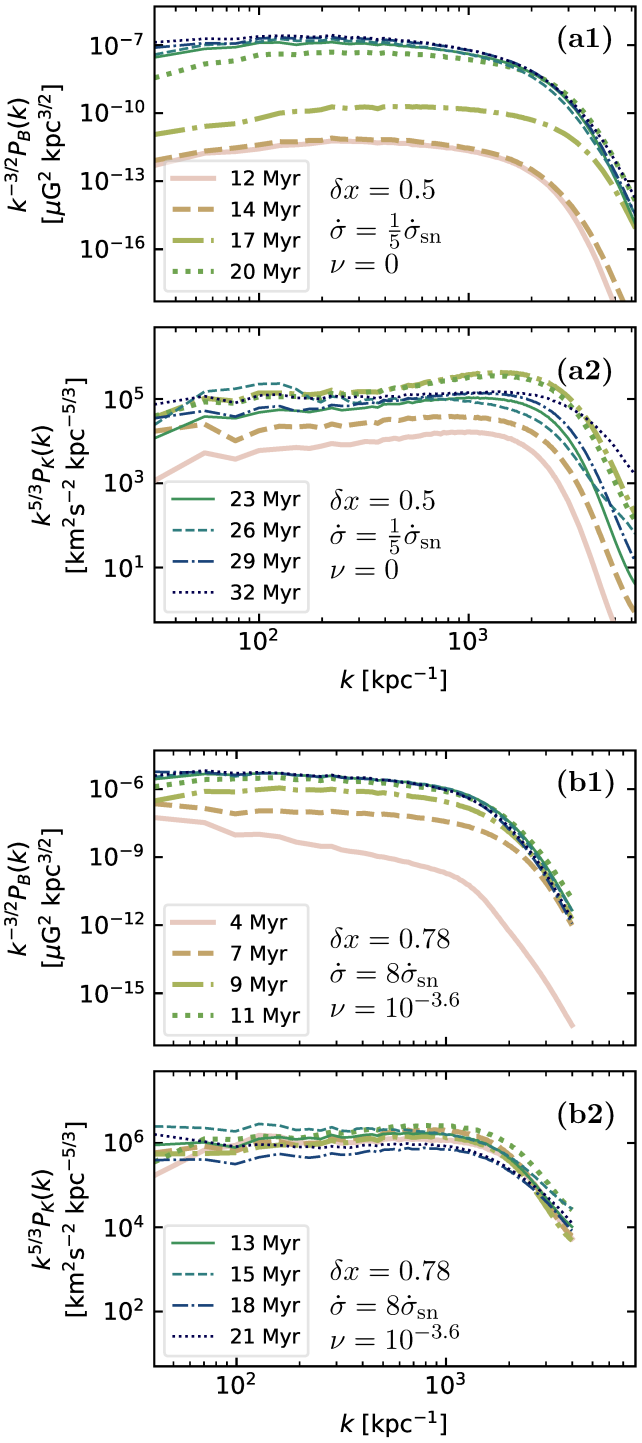

Figure 6. Compensated spectra as in Figure 4 of magnetic (a1, b1) and kinetic (a2, b2) energy at times given in the legends (combined for each pair) for δx, $\dot{\sigma}$ and η indicated. Resistivity is $\eta = 10^{-4}$ with (b1,b2) a comparison to BKMM4.

growth rate and saturation in line with theoretical expectations, there is considerable variation, likely due to intermittency in the multiphase ISM.

4.3. *Tangling of the imposed field*

We now examine whether the field growth seen in our models could be due to tangling. In Sect. 2 we argued that tangling should produce linear growth rate, with dissipation dominating scales below the forcing range. Conversely, an SSD leads to exponential growth and a Kazantsev cascade extending below the forcing scale.

SN-driven turbulence does not have a single forcing scale, because of explosions randomly located in the heterogeneous ISM. Instead, the forcing is distributed at scales of roughly 60–200 pc (Joung & Mac Low 2006; de Avillez & Breitschwerdt 2007; Hollins et al. 2017), or $k \sim 30$–105 kpc^{-1}.

In Figures 3 and 5 we indeed demonstrate strong exponential growth over multiple orders of magnitude for sufficiently low resistivity, at varying supernova rate $\dot{\sigma}$, numerical resolution δx, and physical viscosity ν. Apparently linear growth occurs only with high physical resistivity.

We now turn to the power spectra. Figure 6 shows compensated spectra over time during intervals that span epochs with distinct rates of SSD growth followed by saturation. The compensated magnetic energy spectra in Figure 6 (a1, b1) have peaks conforming to the end of the Kazantsev range.

For $\dot{\sigma} = 0.2\dot{\sigma}_{\rm sn}$ up to 14 Myr this peak is at $k \simeq 200$ kpc^{-1} while the SSD grows slowly. During accelerated growth the Kazentsev range extends to $k \gtrsim 700$ kpc^{-1}, above the forcing scale and consistent with SSD as shown in the uniform, isothermal model (Fig. 1b). The peak contracts upon saturation to $k < 200$ kpc^{-1}, consistent with no further dynamo (Fig. 1c).

In Figure 6 (b1) until 7 Myr there is no Kazantsev range and the peak energy increases

as $k \to 0$, a signature of tangling of the imposed field. However, as the magnetic field grows much larger than the imposed field, this signature disappears and the peak shifts to high k, suggesting a healthy SSD.

We have demonstrated that the magnetic field amplification in BKMM4 is due to SSD. Tangling of the imposed field is initially present, but is dominated by SSD. Our other models with only a weak seed field confirm that an imposed field is not required.

5. CONCLUSIONS

Through the most extensive resolution and parameter study to date, we demonstrate in this Letter that SSD likely occurs easily in the ISM. The critical resistivity is $0.005 > \eta_{\rm crit} \gtrsim 0.001$ kpc km s^{-1} for supernova rate $\dot{\sigma} = 0.2\dot{\sigma}_{\rm sn}$ and increasing over the range considered $\dot{\sigma} \in (0.2\dot{\sigma}_{\rm sn}, 8\dot{\sigma}_{\rm sn})$. The SSD saturates at about 5% of the equipartition kinetic energy density. This level is insensitive to Pm, but increases with increasing Re. We find that the conventional approach from dynamo theory of categorising the turbulence according to Rm based on a forcing scale ℓ, mean random velocity $u_{\rm rms}$ and resistivity η is inadequate for such a complicated system.

We show that simulations with insufficient resolution can appear to converge to a false solution lacking dynamo activity (Fig. 3b). This can occur because these simulations are not scale independent. The SN energy input and the physically motivated ISM cooling processes impose length and time scales that must be adequately resolved. We obtain convergent results for SSD with grid resolution $\delta x \lesssim 1$.

We confirm, by comparing models with and without an imposed magnetic field, that the field amplification obtained in SN-driven ISM turbulence by Balsara et al. (2004) was evidence of an SSD and not only due to tangling of their imposed field. A seed field of less than 1 nG can be amplified to saturation at microgauss levels within about 10 Myr (Figure 3).

Gressel et al. (2008) and Gressel & Elstner (2020) have $\delta x = 8.3$ and 6.7 pc, respectively, and $\eta \simeq 10^{-2.2}$ kpc km s^{-1}, which appears to exclude an SSD. Gent et al. (2013b) with $\delta x = 4$ pc applied $\eta \simeq 10^{-3.1}$ kpc km s^{-1}, which would support SSD for $\dot{\sigma} \simeq \dot{\sigma}_{\rm sn}$. We can now construct LSD experiments to explore how SSD impacts the onset of LSD, critical Ω, and dependence on $\dot{\sigma}$.

ACKNOWLEDGMENTS

We thank O. Gressel and D. Elstner for discussions inspiring this work, and the anonymous referee for comments producing substantial improvement of the presentation. FAG and MJK acknowledge support from the Academy of Finland ReSoLVE Centre of Excellence (grant 307411) and the ERC under the EU's Horizon 2020 research and innovation programme (Project UniSDyn, grant 818665) and computational resources from CSC–IT Center for Science, Finland, under Grand Challenge GDYNS Project 2001062. M-MML was partly supported by US NSF grant AST18-15461.

Software: Pencil Code (Brandenburg & Dobler 2002; Brandenburg et al. 2020)

REFERENCES

Balsara, D. S., & Kim, J. 2005, ApJ, 634, 390

Balsara, D. S., Kim, J., Mac Low, M.-M., & Mathews, G. J. 2004, ApJ, 617, 339

Begelman, M. C., & McKee, C. F. 1990, ApJ, 358, 375

Bhat, P., & Subramanian, K. 2014, ApJL, 791, L34

Brandenburg, A., & Dobler, W. 2002, Computer Physics Communications, 147, 471
Brandenburg, A., & Sarson, G. R. 2002, PhRvL, 88, 055003
Brandenburg, A., Johansen, A., Bourdin, P. A., et al. 2020, arXiv e-prints, arXiv:2009.08231
de Avillez, M. A., & Breitschwerdt, D. 2005, A&A, 436, 585
—. 2007, ApJL, 665, L35
Evirgen, C. C., Gent, F. A., Shukurov, A., Fletcher, A., & Bushby, P. 2017, MNRAS, 464, L105
Falkovich, G. 1994, Physics of Fluids, 6, 1411
Federrath, C., Chabrier, G., Schober, J., et al. 2011, PhRvL, 107, 114504
Federrath, C., Schober, J., Bovino, S., & Schleicher, D. R. G. 2014, ApJL, 797, L19
Fryxell, B., Mueller, E., & Arnett, D. 1991, ApJ, 367, 619
Gatto, A., Walch, S., Mac Low, M.-M., et al. 2015, MNRAS, 449, 1057
Gent, F. A., Mac Low, M.-M., Käpylä, M. J., Sarson, G. R., & Hollins, J. F. 2020, Geophysical and Astrophysical Fluid Dynamics, 114, 77
Gent, F. A., Shukurov, A., Fletcher, A., Sarson, G. R., & Mantere, M. J. 2013a, MNRAS, 432, 1396
Gent, F. A., Shukurov, A., Sarson, G. R., Fletcher, A., & Mantere, M. J. 2013b, MNRAS, 430, L40
Gressel, O., & Elstner, D. 2020, MNRAS, 494, 1180
Gressel, O., Ziegler, U., Elstner, D., & Rüdiger, G. 2008, Astronomische Nachrichten, 329, 619
Hanasz, M., Wóltański, D., & Kowalik, K. 2009, ApJL, 706, L155
Haugen, N. E., Brandenburg, A., & Dobler, W. 2004a, PhRvE, 70, 016308
Haugen, N. E. L., & Brandenburg, A. 2004, PhRvE, 70, 036408
Haugen, N. E. L., Brandenburg, A., & Dobler, W. 2003, ApJL, 597, L141
Haugen, N. E. L., Brandenburg, A., & Mee, A. J. 2004b, MNRAS, 353, 947
Hennebelle, P., & Iffrig, O. 2014, A&A, 570, A81
Hill, A. S., Joung, M. R., Mac Low, M.-M., et al. 2012, ApJ, 750, 104
Hollins, J. F., Sarson, G. R., Shukurov, A., Fletcher, A., & Gent, F. A. 2017, ApJ, 850, 4
Joung, M. K. R., & Mac Low, M.-M. 2006, ApJ, 653, 1266
Korpi, M. J., Brandenburg, A., Shukurov, A., & Tuominen, I. 1999, A&A, 350, 230
Li, M., Ostriker, J. P., Cen, R., Bryan, G. L., & Naab, T. 2015, ApJ, 814, 4
Mac Low, M.-M., Balsara, D. S., Kim, J., & de Avillez, M. A. 2005, ApJ, 626, 864
Pakmor, R., Gómez, F. A., Grand , R. J. J., et al. 2017, MNRAS, 469, 3185
Piontek, R. A., & Ostriker, E. C. 2007, ApJ, 663, 183
Rieder, M., & Teyssier, R. 2016, MNRAS, 457, 1722
Sarazin, C. L., & White, III, R. E. 1987, ApJ, 320, 32
Schekochihin, A. A., Boldyrev, S. A., & Kulsrud, R. M. 2002, ApJ, 567, 828
Schekochihin, A. A., Iskakov, A. B., Cowley, S. C., et al. 2007, New Journal of Physics, 9, 300
Steinwandel, U. P., Beck, M. C., Arth, A., et al. 2019, MNRAS, 483, 1008
Wang, P., & Abel, T. 2009, ApJ, 696, 96
Wolfire, M. G., Hollenbach, D., McKee, C. F., Tielens, A. G. G. M., & Bakes, E. L. O. 1995, ApJ, 443, 152
Zeldovich, Y. B., Ruzmaikin, A. A., & Sokolov, D. D. 1983, Magnetic fields in astrophysics (Gordon & Breach, New York)